Budget of nitrous acid and its impacts on atmospheric oxidative capacity at an urban site in the central Yangtze River Delta region of China

Xiaowen Shi[1], Yifeng Ge[1], Jun Zheng[1*], Yan Ma[1,2], Xinrong Ren[3,4,5], and Yuchan Zhang[1]

[1]Collaborative Innovation Center of Atmospheric Environment and Equipment Technology, Nanjing University of Information Science & Technology, Nanjing 210044, China

[2]NUIST Reading Academy, Nanjing University of Information Science & Technology, Nanjing 210044, China

[3]Air Resources Laboratory, National Oceanic and Atmospheric Administration, College Park, Maryland, USA

[4]Department of Atmospheric and Oceanic Science, University of Maryland, College Park, Maryland, USA

[5]Cooperative Institute for Satellite Earth System Studies, University of Maryland, College Park, Maryland, USA

Correspondence to: Dr. Jun Zheng (zheng.jun@nuist.edu.cn)

Address: School of Environmental Science and Engineering, Nanjing University of Information Science & Technology, Nanjing 210044, China

Tel.: +86-18251919852

Fax: +86-25-58731090

Highlights

- Heterogeneously formed HONO (1.55±1.21ppbv) was commonly observed in YRD, China
- HONO and O_3 photolysis dominated the atmospheric oxidation capability in this study
- Nitrate photolysis was a non-negligible source of HONO in the YRD region of China

Key words: HONO; OH radical; Heterogeneous chemistry; Photolysis of nitrate; Atmospheric oxidative capacity

Abstract

In this study, we used a wet chemistry based long-path absorption spectroscopy method to measure HONO in Changzhou, in the central Yangtze River Delta region (YRD) of China, from April 3-24, 2017. During the observation period, the average HONO mixing ratio was 1.55±1.21 ppbv. In addition, the average OH formation rates of the photolysis of HONO, O_3, HCHO and H_2O_2 along with ozonolysis of alkenes were 7.84×10^6, 2.02×10^7, 7.41×10^5, 3.79×10^5 and 1.51×10^6 molecules cm^{-3} s^{-1}, respectively. At nighttime, the average conversion rate from NO_2 to HONO was determined to be ~0.018 h^{-1}. In this work, the primary emission rate of HONO was determined by the ratios of HONO to nitrogen oxides (NO_x=NO+NO_2) within freshly emitted plumes (NO/NO_x>0.85) and a value of ~0.69% was obtained. The sources of HONO were further investigated through a box model utilizing the Master Chemical Mechanism. The simulation results show that primary emissions contributed only ~12.3% of the total HONO budget during daytime but a substantial portion (31.0%) at night. Comparing to heterogeneous HONO sources, the gas-phase NO+OH reaction was the less important HONO source, with a contribution of 14.2% at night and 28.7% during the daytime. Heterogeneous reactions of NO_2 on various surfaces (mostly the ground surface) were responsible for most of the observed HONO, i.e., 34.7% during the day and 54.4% at night. Overall, nighttime HONO can be reasonably explained by aforementioned mechanisms. However, daytime HONO cannot be fully accounted for without the consideration of nitrate photolysis, which contributed ~24.1% of the daytime HONO according to the model simulation. Our findings highlight that photolysis of particulate nitrate could be an important source of daytime HONO, providing a channel to cycle NO and OH radical back into the photochemical system and further enhancing the atmospheric oxidative capacity within the air shed of a typical industrial zone of China.

1. Introduction

Ever since the first atmospheric detection of nitrous acid (HONO) (Perner and Platt, 1979), HONO chemistry has been demonstrated to be a nonnegligible part of the nitrogen cycle within the relatively polluted urban environments (Alicke et al., 2002; Platt et al., 2002; Stutz et al., 2002). Photolysis of HONO can produce a large amount of hydroxyl radicals (OH), which are the fundamental driving force for the formation of secondary air pollutants. Hence, high concentrations of HONO are often observed concurrently with heavy air pollution episodes (Cui et al., 2018). In addition, studies have found that HONO may exert adverse effects on human health (Jarvis et al., 2005; Sleiman et al., 2010). Therefore, it is of particular importance to accurately determine HONO level in the atmosphere and especially to thoroughly investigate its formation mechanisms under various environments. OH in the atmosphere can be produced through several mechanisms (see the supporting information (SI) for details), of which HONO photolysis (SR1) can proceed within the visible wavelength range and thus is especially enhanced after sunrise (Finlayson-Pitts and Pitts, 1999). Although heavy haze events can substantially reduce ground level solar radiation intensity and thereby may weaken HONO photolysis, recent field observations have indicated that HONO photolysis could be the dominant source of OH radicals (Bernard et al., 2016; Huang et al., 2017; Wang et al., 2017), even larger than the sum of contributions from ozone (O_3) photolysis (SR2 and SR3), photolysis of formaldehyde (HCHO) (SR4 to SR8), and ozonolysis of alkenes (SR9) in some heavily polluted areas (Elshorbany et al., 2009; Li et al., 2018). Hydrogen peroxide (H_2O_2) is also ubiquitous in the atmosphere and can be photolyzed to produce OH radicals

(SR10). However, H_2O_2 is nearly two orders of magnitude less photosensitive than HONO or HCHO and the typical ambient H_2O_2 concentration is around several ppbv (He et al., 2010). Therefore, even given similar ambient concentrations of H_2O_2 as HONO and HCHO (e.g., several ppbv), H_2O_2 Phphotolysis is not expected to contribute significantly to OH budget, which is demonstrated in the following discussion.

Although HONO can heavily impact atmospheric chemical processes, the sources of HONO in the atmosphere and the underlying HONO formation mechanisms have not been fully understood, the strength of which can vary substantially in different environments (VandenBoer et al., 2014). Currently, the major primary sources of HONO include emissions from incomplete combustion processes, such as vehicle exhaust (Kirchstetter et al., 1996; Kurtenbach et al., 2001; Liang et al., 2017; Nakashima and Kajii, 2017; Trinh et al., 2017; Xu et al., 2015) and biomass burning (Müller et al., 2016; Neuman et al., 2016; Nie et al., 2015; Rondon and Sanhueza, 1989). Besides direct emissions, HONO is believed to be mainly originated from secondary formation. A common mechanism is the gas-phase homogeneous reaction, i.e., the combination reaction of nitric oxide (NO) and OH:

$$\mathrm{NO + OH \rightarrow HONO} \qquad \text{(R1)}$$

When only the photo-stationary state (PSS) involving Reaction R1 is considered, daytime HONO concentration could be seriously underestimated (Kleffmann et al., 2005; Michoud et al., 2014). It has been strongly suggested that the missing daytime HONO source is related to NO_2 and light (Lee et al., 2016).

Moreover, heterogeneous reactions of nitrogen dioxide (NO_2) on various surfaces have been proposed to be the most likely source of HONO under most circumstances (Huang et al., 2017). Laboratory studies have shown that NO_2 can be converted to HONO on a wet surface (R2),

$$\mathrm{2NO_{2(g)} + H_2O_{(ads)} \rightarrow HONO_{(g)} + HNO_{3(ads)}} \qquad \text{(R2)}$$

the formation rate of which depends critically on the uptake coefficient of NO_2 on the type of the reaction surface and the surface area density (Finlayson-Pitts et al., 2003; Kleffmann et al., 1998). Soot particles emitted from diesel exhaust have been regarded as a more promising substrate for heterogeneous reactions of NO_2 (Ammann et al., 1998; Gerecke et al., 1998; C. Han et al., 2017; Monge et al., 2010) and semi-volatile organic compounds adsorbed on the soot surface are believed to be able to react with NO_2 at a much faster rate than that of water (George et al., 2005; Gutzwiller et al., 2002). During daytime, these heterogeneous reactions can also be enhanced by solar radiation, such as photo-enhanced reactions of NO_2 on the surface of dust (Ndour et al., 2008), humic acid, and ground surfaces (Chong Han et al., 2017; Wall and Harris, 2016). Moreover, field observations and laboratory simulations have strongly suggested that photolysis of adsorbed nitric acid (HNO_3) and particulate nitrate (NO_3^-) may also contribute significantly to HONO formations (Ye et al., 2016; Ye et al., 2017; Zhou et al., 2002; Zhou et al., 2003; Zhou et al., 2011; Ziemba et al., 2010).

$$HNO_3/NO_3^- + h\nu \rightarrow HONO/NO_2^- + O \qquad \text{(R3)}$$

The Yangtze River Delta (YRD) region is one of the most developed regions in Eastern China and contributes more than one third of the industrial production of China. In the past 30 years, rapid urbanization and industrialization have led to severe deterioration of air quality in this region, characterized by high concentrations of ozone (O_3) and particulate matters ($PM_{2.5}$). Previous studies have often focused on the more populated metropolitan areas in this region, such as Shanghai and Nanjing, which are considerably far away from the industrial zones that are essentially responsible for the formation of air pollution events (Cui et al., 2018; Nie et al., 2015). Changzhou, on the other hand, is located in the central YRD region and is the home of most typical industrial activities encountered in this region, such as power generation, petrochemical refinements, steel mills, along with the domestic activities. Therefore, it provides a more representative environment to fully elucidate the mechanism underlying the air pollution formation in the YRD region.

In this study, we conducted a suite of measurements, including HONO and other particulate/gas-phase air pollutants at the Changzhou Environmental Monitoring Center from April 3 to 24, 2017. The potential mechanism of HONO formation was investigated using a Master Chemical Mechanism (MCM) box model. Our results may provide firsthand insights into the characteristics of air pollution in the YRD region, and help the authorities to develop more effective air pollution mitigation strategies.

2. Experimental methods

2.1. Observation site

This study was conducted at the Changzhou Environmental Monitoring Center (119.9° E and 31.8° N) (see Fig. S1 for the map of the site) from April 3 to 24, 2017. All instruments used in the measurements were placed on the top floor of a three-story academic building and the sampling inlets were installed on the rooftop, roughly 2 m above the roof surface to minimize surface effects. There were no industrial activities and major highways near the study site. Unlike the over-populated super-megacities (e.g., Shanghai, Nanjing and Hangzhou), Changzhou was characterized as a medium-sized city (i.e., ~3.3 million population) with moderate domestic activities and related emissions. Nevertheless, the site was occasionally expected to be influenced by industrial emissions due to transport.

2.2. HONO measurement

HONO was measured using a custom-built liquid-waveguide long-path absorption spectroscopy instrument, a wet chemistry based technique developed by Ren et al. (2010), with a detection limit of 3 pptv and a time resolution of 2 min. Figure S2 is a schematic diagram of the HONO instrument and the detailed description of the instrument is provided in the supporting information (SI).

In this study, the instrument was calibrated regularly with standard concentrations of sodium nitrite ($NaNO_2$) solution to determine the response of the instrument. The mixing ratio of gaseous HONO in the sampled air can be calculated using the following equation (1) (Ren et al., 2010):

$$[\mathrm{HONO}]_{\mathrm{pptv}} = \frac{\mathrm{C_l F_l R T}}{\mathrm{F_g P}} \times 10^{12} \tag{1}$$

where C_l is nitrite concentration (mol L^{-1}) in the scrubbing solution, F_l is the liquid flow rate (mL min^{-1}) of the scrubbing solution, F_g is the sampling air flow rate (L min^{-1}), R is the ideal gas constant (8.314 m^3 Pa K^{-1} mol^{-1}), and T and P are the ambient temperature (K) and atmospheric pressure (Pa), respectively.

Currently, other major HONO measurement techniques include long path differential UV absorption spectrometer (LP-DOAS), incoherent broadband cavity-enhanced absorption spectroscopy (IBBCEAS) (Nakashima and Kajii, 2017), and cavity-enhanced absorption spectrometer (CEAS) (Scharko et al., 2017). These spectroscopic techniques have the advantage of high sensitivities but normally require relatively clean operation environments for their delicate optical parts. Our wet-chemistry based method, on the other hand, is essentially the same the long path absorption photometer (LOPAP) instrument (Heland et al., 2001), with the advantages of a fast time resolution and a high sensitivity (down to a few pptv).

2.3. Other measurements

In addition to HONO, trace gases and meteorological parameters (e.g., wind direction (WD), wind speed (WS), ambient temperature (T), air pressure (P), and relative humidity (RH)) were also simultaneously measured. NO/NO_2, carbon monoxide (CO), sulfur dioxide (SO_2), and ozone (O_3) were respectively measured with Thermo Scientific gas analyzers Models 42i, 48i, 43i and 49i, respectively.

Fine particle ($PM_{2.5}$) mass concentration was acquired from an online instrument (MET ONE, BAM-1020), with a time resolution of 1 hour. The aerosol number size distribution (5 nm-10 μm) was measured by a wide particle spectrometer (WPS) (MSP, Model 1000 XP) with a time resolution of 5 minutes. In this study, HCHO and other volatile organic compounds (VOC) were measured with a custom-built proton transfer reaction ion-drift chemical ionization mass spectrometer (PTR-ID-CIMS), which has been described in details in our previous work (de Gouw and Warneke, 2007; Ma et al., 2016). However, alkanes cannot be detected by the PTR-ID-CIMS and thus were not used in this work. During our earlier study near an industrial park in Nanjing, we found that on average alkanes only contributed about ~4.5% of OH reactivity of the total VOC population (Zheng et al., 2019). Therefore, we concluded that omission of alkanes in this work would not cause significant uncertainty in the MCM box model simulations. NO_3^-, organic matters and other aerosol components were measured by an Aerodyne aerosol chemical speciation monitor (ACSM). Black carbon (BC) was measured by an AE-31 Aethalometer (Magee Scientific Inc.) with a time resolution of 5 minutes. Solar actinic flux (285 nm-650 nm) and photolysis frequencies, including $J(O^1D)$, $J(NO_2)$, J(HONO), $J(H_2O_2)$, J(HCHO) and $J(NO_3)$, were measured by a commercial radiometer with an ultra-fast charged coupled device (CCD) detector (Meteorology Consult Gmbh, Germany) with a time resolution of 1 minute. Other photolysis frequencies (eg, carbonyl compounds containing more than two carbons) are calculated according to the following equation (Jenkin et al., 1997)):

$$J_i = L_i \cos(\chi)\, M_i \exp(-N_i \sec(\chi)) \qquad (2)$$

where χ is the solar zenith angle; L_i, M_i and N_i are photolysis parameters and are taken from Jenkin et al. (1997), for clear sky conditions. The calculated photolysis frequencies were then scaled by the measured $J(NO_2)$ for cloudiness correction.

The detailed measurement time-resolution and measurement uncertainty of each instrument used in this work have been included in Table S3 of the SI.

2.4. Boundary layer height

The boundary layer (BL) height used in this work was obtained from the vertical sounding measurements network (http://envf.ust.hk/dataview/profile/current/). Since no direct sounding measurements were available at the Changzhou site during the observation period, the monthly-averaged BL heights measured at Nanjing and Shanghai of the same longitude as Changzhou were used in this work. Diurnally, the BL started to develop after sunrise (~8:30 LT) and reached the daily maximum of 595 m in the early afternoon. After that the BL height decreases gradually to the lowest of 75 m at night (see Fig. S3 for details).

2.5. MCM model simulation

In this study, a Master Chemical Mechanism (MCM V3.3.1) (Jenkin et al., 2015) box model was used to simulate the HONO chemistry, operated through a commercial software (FACSIMILE 4.0, UES Software Inc.). The kinetic rate coefficients used in the model were taken from the MCM website (http://mcm.leeds.ac.uk/mcm/). During model simulations, HONO, O_3, NO_x, CO, SO_2, HCHO and other VOC were used as input parameters to obtain the equilibrium concentrations of OH, HO_2 and other reactive substances.

A Monte Carlo sensitivity analysis was also conducted to assess the model performance. In each Monte Carlo simulation, the input variables of the model, including HONO, O_3, NO, NO_2, CO, SO_2, HCHO, VOCs, reaction rate constants and photolysis frequencies, were independently set to vary within ±10% of the mean value of individual variable with a normal probability distribution.

3. Results and discussion

3.1. Data overview

3.1.1. Time series

The time series of meteorological data and concentrations of the air pollutants during the observation period are shown in Fig. 1. The temperature during the observation period ranged from 8.7 °C to 32.1 °C, with an average of 18.7 ± 4.8°C; the RH ranged from 13% to 86%, with an average of 53.7 ± 19.8%. The wind direction during the observation period was dominated by the westerly wind and the wind speed ranged from 0.2 to 4.5 m s^{-1}, with an average of 1.4 ± 0.4 m s^{-1}. The weather was mostly clear during the observation period with several relatively strong precipitation events around April 6, 9, 10 and 17.

The observed HONO was between 0.01ppbv and 8.07 ppbv, with an average of 1.55 ± 1.21 ppbv. The concentrations of NO, NO_2, O_3, CO and $PM_{2.5}$ were 0.7-80.6ppbv, 2.1-103.7 ppbv, 0.5-127.3 ppbv, 0.8-4.5 ppmv and 22-138 μg m^{-3}, respectively (see Table S1 for details). Table S2 lists recent HONO observations measured in China. The observed HONO levels in this study are comparable to the HONO levels observed in summer of Beijing in 2015 (Wang et al., 2017) but higher than those observed in Xianghe, Beijing (Hendrick et al., 2014; Spataro et al., 2013), Jinan (Wang et al., 2015), Hong Kong (Xu et al., 2015), Shanghai (Wang et al., 2013) and Xinken (Su et al., 2008). However, the HONO concentrations we observed are substantially lower than those observed in Beijing in autumn of 2015 (Wang et al., 2017). The general trends of NO_x, CO and BC are very similar, indicating primary emissions from motor vehicles might play an important role in the study area. Although the ACSM can only measure $PM_{1.0}$, nitrate followed $PM_{2.5}$ very well, indicating that most portion of the $PM_{2.5}$ mass may reside in the accumulation mode. Particulate nitrate can be formed either through the gas/particle partitioning process of gaseous HNO_3 that is photochemically produced in the atmosphere (R4 and R5) or by heterogeneous reaction of dinitrogen pentoxide (N_2O_5) with water on the particle surfaces (R6 to R8) (Finlayson-Pitts and Pitts, 1999).

$$OH + NO_2 \rightarrow HNO_{3\,(gas)} \qquad (R4)$$

$$HNO_{3\,(gas)} \leftrightarrow NO_3^-{}_{(aerosol)} \qquad (R5)$$

$$NO_2 + O_3 \rightarrow NO_3 \qquad (R6)$$

$$NO_3 + NO_2 \rightarrow N_2O_5 \qquad (R7)$$

$$N_2O_5 + H_2O \rightarrow 2HNO_{3(aerosol)} \qquad (R8)$$

The average nitrate concentration at this site was 8.12 ± 7.11 $\mu g/m^3$, which was equivalent to ~3 ppbv of gaseous HNO_3 under standard conditions. Meanwhile, the average NO_x concentration was about 31.1 ± 19.7 ppbv. Given the relatively mild ambient temperature (< 20 °C), it was reasonable to assume that most portion of HNO_3 was in the aerosol phase, i.e., particulate nitrate can be roughly used to represent the level of oxidized nitrogen species (NO_z). NO_x was nearly 10 times higher than NO_z, indicating that the NO_x plume was relatively fresh and had not been photochemically aged, excluding the possibility of long-range transport. Accordingly, the most likely source of NO_x was local automobile exhaust. In addition, since the nighttime O_3 was depleted by the freshly emitted NO_x plumes (see Fig. 1), the nighttime N_2O_5 chemistry (R6 and R7) was not likely to proceed at a significant level. Particulate nitrate was largely produced from local photochemical process.

3.1.2. Diurnal variations

The diurnal variations of NO_2, NO_x, HONO, aerosol surface density (S/V), particulate nitrate (NO_3^-) and the ratio of HONO to NO_2 ($HONO/NO_2$) are shown in Fig. 2. Both NO_2 and NO_x clearly show traffic rush-hour peaks around 06:00-07:00 and 19:00-20:00 (Beijing Time) as we expect in typical urban environments. Both HONO and aerosol surface density only show moderate traffic influence. However, the fact that HONO correlates well with S/V with a correlation coefficient of 0.80 (see Fig. S4) suggests HONO production may be strongly affected by heterogeneous chemistry mechanisms on aerosol surfaces, although ground surfaces cannot be ruled out. Recently, near ppbv levels of daytime HONO have been often observed in polluted areas (Cui et al., 2018; Li et al., 2018; Qin et al., 2009). The distinct HONO/NO_2 peak around noontime indicated that in this work daytime HONO was not only high but also was converted from NO_2 more efficiently under strong solar radiation, which was in favor of photo-sensitized and/or enhanced HONO formation mechanisms.

3.2. OH radical simulation

HONO chemistry has drawn more and more attention due to its high photo-sensitivity and high ambient concentrations of HONO have been detected within most of the urban environments with deteriorating air quality (Elshorbany et al., 2009; Hendrick et al., 2014; Kleffmann et al., 2005; Su et al., 2008). HONO photolysis can contribute considerably to the atmospheric oxidation capacity by acting as an OH source, which in turn can initiate chain reactions to oxidize VOC and other primary air pollutants into secondary pollutants. Through these reactions, secondary oxidants (e.g., O_3 and NO_3) and other peroxyl radicals (e.g., HO_2 and RO_2) are also formed. Meanwhile, OH can be regenerated by NO_x cycling (Atkinson and Arey, 2003) or other processes even without the presence of adequate NO_x (Rohrer et al., 2014). Therefore, OH radical is the ultimate oxidant in the atmosphere, controlling the lifetime of most of the air pollutants. Nevertheless, recent field studies indicated that the effective coupling of RO_x (i.e., OH + HO_2 + RO_2) and NO_x cycles can lead to rapid formations of secondary pollutants (Tan et al., 2018). A full knowledge of OH chemistry in the atmosphere is essential for understanding atmospheric oxidative capacity and establishing an effective air pollution mitigation strategy. Despite the importance of OH radical, in-situ measurements of OH is difficult to achieve due to the high reactivity and hence extreme low ambient abundance of OH (on the orders of 10^6 to 10^7 molecules cm^{-3}). The few available OH measurement techniques can also suffer from considerable interferences and may be associated with fair amount of measurement uncertainties (Ren et al., 2004; Tanner and Eisele, 1995). Laser induced fluorescence (LIF) based techniques are currently the most widely used OH measurement instrument

(Fuchs et al., 2008; Fuchs et al., 2011; Ren et al., 2004). In recent field studies, the observed OH concentrations generally agree well with the model-simulated OH profile. The OH concentrations measured at various places under different environments also showed comparable diurnal ranges, on the orders of 10^6 to 10^7 molecules/cm^3 (Dusanter et al., 2009; Petaja et al., 2009; Ren et al., 2003; Tan et al., 2018). These results suggest that OH production is normally well balanced by its loss in the atmosphere. Under relatively polluted conditions, the photochemical activity is more efficacious but meanwhile the higher pollutants concentration will also provide additional OH sinks. In theory, the atmospheric oxidative capacity can be controlled by regulating OH radical sources (i.e., the rate of OH formation) without knowing the exact OH radical concentration. Accordingly, box models are often employed instead to simulate the behavior of these highly reactive species, especially to explore the sensitivity of OH to the variations of its precursors. It is worth noting that while modeling environments with elevated NO_x conditions models tend to significantly underestimate OH level, particularly in China (Ma et al., 2019; Tan et al., 2017). Therefore, the OH concentration used here may be treated as a lower limit.

To assess the relative contributions of potential OH sources in this study, we used a box model, based on the Master Chemical Mechanism (MCM V3.3.1) (Jenkin et al., 2015), to simulate OH concentration and the production rate of OH from different sources. Model simulations were constrained by the aforementioned measurement results. Figure S5 shows the time series of simulated OH radical and observed HONO photolysis rates. Since the model was constrained by the in situ observations, the simulations were only performed during the time periods when all data sets were available. The highest concentration of OH is 1.83×10^7 molecules cm^{-3}, and the daytime average is about $4.1\pm3.7\times10^6$ molecules cm^{-3}. This result is within the range observed in Guangzhou (Lu et al., 2012) and Beijing (Tan et al., 2018). The relatively higher OH level in Guangzhou than that observed in Beijing is most likely due to the difference in solar radiation intensity, i.e., summer time Guangzhou vs wintertime Beijing. Also showed in Fig. S5 is the HONO photolysis rate. OH clearly follows the HONO photolysis rate very closely as expected.

3.3. OH formation rate

The magnitudes or the relative contributions of different OH sources were represented by their corresponding OH formation rates calculated according to Eqs. SE1-SE6, which were derived from Reactions SR1 to SR10. The second term in Eq. SE1 is the loss of OH due to the homogeneous reaction of OH + NO to reproduce HONO, i.e., some of the OH from the HONO photolysis will recombine with NO to regenerate HONO. Each J value is the photolysis frequency of the corresponding species, and φ_{OH} is the fraction of $O(^1D)$ reacted with water rather than quenched by nitrogen (N_2) or oxygen (O_2). Here, in calculating the OH produced by photolysis of formaldehyde, it is assumed that in a polluted environment HO_2 generated by the Reaction SR4 is immediately converted into OH by the Reaction SR8 due to high NO levels. In Eq. SE6, $\mathrm{Yield}_{\mathrm{OH}}$ is the yield of OH produced by the gas phase reaction of O_3 with alkene(i) and $k_{alkene(i)+O_3}$ is its reaction rate constant. Table S4 lists the rate constants for the ozonolysis reaction and the corresponding OH yields used in this study. Since H_2O_2 was not measured during this observation, H_2O_2 was estimated based on literature values, 0.5 ppbv-5 ppbv (Guo et al., 2014; Hua et al., 2008; Ren et al., 2009), and in this work a constant mixing ratio of 3 ppbv H_2O_2 was used in the simulations.

The calculated contributions from photolysis of HONO, O_3, HCHO, H_2O_2 and ozonolysis of alkenes to daytime (06:00-18:00) OH production rates during the entire observation period are shown in Fig. S6. The average OH formation rate of the photolysis of HONO, O_3, HCHO and H_2O_2 along with ozonolysis of alkenes are 7.84×10^6, 2.02×10^7, 7.41×10^5, 3.79×10^5 , and 1.51×10^6 molecules cm^{-3} s^{-1}, respectively (see Table S5). Overall, the photolysis of O_3 dominated the OH production. However, HONO photolysis also played an important role in OH production, especially during the early morning hours, which can also significantly impact the formation of O_3 and other secondary pollutants. To accurately evaluate the impacts of HONO chemistry on O_3 formation, a more comprehensive three-dimensional model, driven by a detailed meteorological field and emission inventories (e.g., a weather research and forecasting model coupled with Chemistry (WRF-CHEM)), is needed to fully address both chemical and physical processes that may affect local O_3 concentration, which is beyond the scope of this work. For example, based on WRF-CHEM simulations Li et al. (2010) have demonstrated that in Mexico City high HONO level can both accelerate O_3 formation rate and increase peak O_3 concentration in the afternoon. Therefore, HONO can indirectly be responsible for part of the OH formation from O_3 photolysis. From April 5-8, HONO photolysis dominated the OH production throughout the daytime. During these days, high cloud coverage significantly reduced ground level photochemistry (see J(HONO) in Fig. 1), thus O_3 concentration was substantially suppressed. HONO, on the other hand, can still be produced and was likely to accumulate under dark conditions and thus may reach relatively high concentrations. During haze events, all photolysis rates will be lower, including that of NO_2, O_3, HCHO and HONO. However, since both NO_2 and HONO concentrations are higher during haze events, HONO photolysis may become the major OH source with respect to other OH sources although the total magnitude of OH formation rate during haze events may be reduced. Meanwhile, $PM_{2.5}$ also remained elevated, indicating that secondary air pollutants formation can still be sustained. These observation indicate that in order to effectively mitigate air pollutions formation in the YRD region, it is crucial to fully understand the potential OH sources, i.e., OH precursors.

3.4. Primary HONO emissions

The observation site was located in an urban environment and was affected by local vehicle emissions as indicated by Fig. 2. In this study, freshly emitted vehicle plumes were defined as: a) $NO_x > 40$ ppbv; b) $\Delta NO/\Delta NO_x > 0.85$; c) good correlation between HONO and NO_x ($r > 0.9$); d) short duration (≤ 2 hours); e) $J(NO_2) \leq 2.5\times10^{-4}\ s^{-1}$. Figure S7 shows the time series of dNO/dNO_x (in 5 min intervals) and the correlation between HONO and dNO/dNO_x. A moderate correlation between HONO and dNO/dNO_x ($r = 0.38$) can be found, indicating that primary emissions may contribute significantly to HONO budget but was not likely the dominant HONO source. According to the aforementioned criteria, five periods were chosen from the time series of dNO/dNO_x (labeled with red letters in Fig. S7) and the corresponding HONO emission factor (EF), i.e., the $\Delta HONO/\Delta NO_x$ ratio was evaluated following the method of Xu et al. (2015). The detailed information of the five fresh plumes were listed in Table 1 and the corresponding correlation plots of NO vs NO_x were shown in the inserts of a to e in Fig. S7). The average $\Delta HONO/\Delta NO_x$ ratio was determined to be $0.69 \pm 0.48\%$. HONO EF can vary substantially due to the difference in combustion conditions; the type of fuel used (e.g., gasoline or diesel) (Kurtenbach et al., 2001), and so on. In addition, secondary formation of HONO can also contribute to the increase of HONO concentration within these plumes. Comparing to recent studies, especially those in China, our EF value was significantly lower. For example, Liang et al. (Liang et al., 2017) obtained an EE of 1.24% during a tunnel experiment in Hong Kong, where diesel fueled vehicles consisted of 38% of the fleet, significantly higher than what we found in Changzhou, and thus may lead to a higher EF value. In another study during Beijing haze events, Zhang et al. (2019) found that primary emissions dominated HONO budget with a EF of 1.2%. The NO concentration observed by Zhang et al. (2019) was much higher than this study. However, HONO formation due to both homogeneous reaction (OH+NO) and surface heterogeneous reactions during heavy pollution episodes (i.e., high NO and high PM loading) as encountered in Beijing might also lead to more prominent positive bias on the EF determination. More recently, Kramer et al. (2019) reported tunnel experiment results (EF of 0.72-1.01%) in Birmingham, UK, where 59% of its vehicle fleet was consisted of diesel fueled vehicles. This may explain to some extent the relatively higher HONO EF values than our study. These studies suggest that EF can be specific to a particular environment, i.e., of a specific fleet composition and under a certain driving condition. In this study, the mean EF of 0.69% was used to calculate the contribution of direct emission to HONO budget, defined as $\mathrm{HONO}_{\mathrm{emis}}$, which should be considered as an upper limit of the estimated HONO emission.

$$\mathrm{HONO}_{\mathrm{emis}} = \mathrm{NO}_x \times 0.0069 \tag{3}$$

On average, the primary emissions from vehicle exhaust accounted for 31.0% of the total HONO concentration at night but substantially less during daytime (12.3%), indicating secondary mechanisms still dominated HONO level in the study area, which will be further analyzed in the following sections.

3.5. HONO formation

3.5.1. Conversion ratio of NO_2 to HONO

Generally, HONO is believed to be primarily converted from NO_2. The conversion ratio is typically used as an indicator for the HONO formation efficiency (Stutz et al., 2002). In order to eliminate the influence of primary emissions on the evaluation of the secondary formation of HONO, the observed HONO was corrected by removing the portion of primary emissions ($HONO_{emis}$) and was denoted as $HONO_{corr}$:

$$\mathrm{HONO_{corr}} = \mathrm{HONO} - \mathrm{HONO_{emis}} \tag{4}$$

Accordingly, the conversion rate of NO_2 to HONO (C_{HONO}) at nighttime can be calculated as (Alicke et al., 2003):

$$C_{HONO} = \frac{[HONO_{corr}]_{t_2} - [HONO_{corr}]_{t_1}}{(t_2 - t_1)[\overline{NO_2}]} \tag{5}$$

where $[HONO_{corr}]_{t1}$ and $[HONO_{corr}]_{t2}$ are the corrected HONO concentrations at two sequential data points, t_1 and t_2, respectively, $[\overline{NO_2}]$ is the average NO_2 concentration between time t_1 and t_2. Although no certain value of C_{HONO} can be specifically associated with certain NO_2 conversion mechanism, the magnitude of C_{HONO} may be used as an indicator of the efficiency of the underlying HONO formation route. The average C_{HONO} obtained in this study is about 0.018 h^{-1}, which is within the range of reported values in urban and suburban areas (0.004 ~ 0.024h^{-1}) (Acker et al., 2006; Li et al., 2012; Wang et al., 2017; Wang et al., 2013).

3.5.2. Surface HONO formation

Previous studies have demonstrated that the heterogeneous reaction of NO_2 on the surface is a first-order reaction (Finlayson-Pitts and Pitts, 1999), and it can be expressed as the following equations (Li et al., 2010):

$$NO_2 \xrightarrow{k_a} HONO, \tag{R9}$$

$$NO_2 \xrightarrow{k_g} HONO, \tag{R10}$$

where k_a and k_g are the first-order rate constants for HONO conversions on aerosol and ground surfaces, respectively. In the box model, k_a is calculated using the following formula:

$$k_a = \frac{{}_{NO2,aerosol}\overline{v}(S/V)}{4} \tag{6}$$

where $\bar{v}$ is the root mean square (RMS) velocity of NO_2 molecule, S/V is the aerosol surface area density and $\gamma_{NO2,aerosol}$ is the reactive uptake coefficient of NO_2 on the aerosol surface, a value of 8×10^{-6} is used under dark conditions (VandenBoer et al., 2013). At daytime, however, significant enhancement of NO_2 conversion to HONO has been found for various types of aerosol surfaces, such as humic acid and similar organic materials (Stemmler et al., 2007), soot (Monge et al., 2010) and mineral dusts (Ndour et al., 2008). Accordingly, to account for the photo-enhancement, a photo-enhanced uptake coefficient of 2×10^{-5} (Zhang et al., 2016) was used in this work around the morning hours (~09:00) and was scaled by the measured photolysis rate of NO_2, i.e., $(JNO_2)/5\times10^{-3}$ for J_{NO2} higher than 5×10^{-3} (the value of J_{NO2} at ~09:00) (Li et al., 2010).

$$k_g = \frac{V_{d,NO2}}{2H} \qquad (7)$$

$$V_{d,NO2} = \frac{_{NO2,ground}\bar{v}}{4.2} \qquad (8)$$

Eqs. (7) and (8) is used to calculate k_g, where $V_{d,NO2}$ represents the deposition velocity of NO_2, H is the boundary layer height (detailed in Fig. S3) and $\gamma_{NO2,ground}$ is the uptake coefficient of NO_2 on the ground surface. Here, the nighttime uptake coefficient of NO_2 on the ground surface was taken as 1×10^{-5} (Trick, 2004) and it was increased to 6×10^{-5} (Wong et al., 2012) during the day to account for the photo-enhancement, similar to the case on the aerosol surfaces, the same scale factor $J(NO_2)/(5\times10^{-3})$ was also applied to the heterogeneous reaction on the ground surface during the day.

3.5.3. Photolysis of nitrate

The portion of HONO generated from nitrate photolysis is calculated as the following (Liu et al., 2019):

$$\mathrm{HONO}_{\mathrm{NO_3^-}\rightarrow\mathrm{HONO}} = [\mathrm{NO_3^-}]\times\frac{\mathrm{RT}}{\mathrm{MP}}\times \mathrm{J}_{\mathrm{NO_3^-}}\times10^3\times3600 \qquad (9)$$

where $\mathrm{HONO}_{\mathrm{NO_3^-}\rightarrow\mathrm{HONO}}$ (ppbv/h) is the simulated HONO concentrations from photolysis of particulate nitrate, $[NO_3^-]$ is the observed particulate nitrate mass concentration (μg/m^3), R is the ideal gas constant (8.2×10^{-5} m$^3\cdot$atm/(K$\cdot$mol)), P is the pressure (atm), T is the temperature (K), M is the molecular weight of nitrate (g/mol) and J_{NO3}^- is the photolysis frequency of particulate nitrate. The reported value of J_{NO3}^- ranges from 6.2×10^{-6} to 5.0×10^{-4} s^{-1}, with a median of 8.3×10^{-5} s^{-1} at noontime (Ye et al., 2017). To account for the diurnal variation of solar radiation, we normalized J_{NO3}^- by the photolysis rate of HNO_3, J_{HNO3}, which should possess a similar wavelength dependency as J_{NO3}^- but associate with a much smaller value (~7×10^{-7} s^{-1} at noontime). Therefore, we adopted the same methodology as that of Sarwar et al. (2008), i.e., J_{NO3}^- was scaled by J_{HNO3} as the following:

$$J_{NO_3^-} = \frac{8.3\times10^{-5}}{7\times10^{-7}} \times J_{HNO_3} \tag{10}$$

3.5.4. HONO simulation

In the box model, the aforementioned HONO sources have been summarized in Table 2. In addition, the following major HONO loss processes were also considered: 1) photolysis of HONO; 2) the homogeneous reaction of HONO with OH; 3) the dry deposition of HONO on the ground, i.e., $\frac{v_{HONO}}{H}[HONO]$, where v_{HONO} is the dry deposition velocity of HONO, taken as 0.48 cm s^{-1} (Lee et al., 2016); H is the boundary layer height.

We have first investigated the role of nitrate photolysis on a particular high nitrate loading day, i.e., April 5. The simulation results are shown in Fig. 3 along with the hourly averaged diurnal profile of measured HONO (black dots). In general, the nighttime simulation results agree fairly well with the observation and ground surface appears to be the dominant HONO source followed by the primary emissions. During daytime, however, the simulated HONO clearly does not match the observation without the contribution from nitrate photolysis. Specifically, the fine structure of observed HONO can be described by the photolysis of nitrate. For example, the HONO peaks around 9:00 AM and 10:30 AM also can be reproduced by the nitrate photolysis, which strongly supported the assumption that nitrate photolysis was an important daytime source of HONO.

We further applied the nitrate photolysis into the model simulation for the entire campaign period. The simulation results are plotted into Fig. 4a. The main sources of HONO at night (18:00-06:00) were still the heterogeneous reaction of NO_2 on the ground surfaces and direct emissions. After sunrise, as the light intensity increased, photo-enhanced ground surface reactions, nitrate photolysis and the gas-phase reaction became more and more important. The gas phase reaction (NO + OH) contributed a small portion to the HONO formation during the day (06:00-18:00) (~28.7% ± 8%). On the other hand, the nitrate photolysis accounted for a large part of daytime HONO (~24.1% ± 13%). The contribution of nitrate photolysis was the largest at ~09:00, with an average of 0.60 ppbv and dropped to 0.02 ppbv around 18:00. Nevertheless, the daytime HONO can be accounted for by including the nitrate photolysis to a large extent. A Monte Carlo sensitivity analysis was also conducted to assess the model simulation uncertainty of HONO concentration (green marker in Fig. 4a). For each of the 24 hours, 100 independent runs were performed. The Monte Carlo sensitivity analysis show that the model uncertainty of HONO ranged from ±14.0% to ±29.2%. In addition, from the sensitivity test of each individual parameter used in the model (i.e., varying a single parameter by ±10% while keeping the others constant), HONO was found to be mostly sensitive to the photolysis rate of particulate nitrate, $J_{NO_3^-}$, during daytime (±3.3%) and the NO_2 uptake coefficient, $\gamma_{NO2,ground}$, during nighttime (±4.2%), respectively. Morever, we have conducted extra sensitivity tests specifically on the nitrate photolysis rate, within the upper and lower range reported by Ye et al. (2017), i.e., ranging from 6.2×10^{-6} to 5×10^{-4} s^{-1}. The results (see Fig. S8) show that at the upper bound HONO will only increase by 0.25 ppbv but when the lower bound was used nitrate photolysis almost contributed no HONO at all, comparing to the medium case (8.3×10^{-5} s^{-1}) used in this work. The possible reason is that the nitrate photolysis rate is much less than that of HONO. Most of the increased HONO will be photolyzed and thus HONO concentration will not increase proportionally to that of nitrate photolysis rate. These sensitivity analyses reinforced the conclusions that the proposed HONO sources can generally capture the observed HONO trend. Figure 4b is the diurnally averaged contributions of different sources to the HONO budget during the campaign period based on the same simulation results as Fig. 4a. On average, direct emission, gas-phase NO+OH reaction, heterogeneous reactions of NO_2 on various surfaces and nitrate photolysis contributed 12.3% ,28.7%,34.7%, and 24.1% of the total daytime HONO (6:00-18:00); at night, direct emission, gas-phase NO+OH reaction and heterogeneous reactions of NO_2 contributed 31.0% ,14.2%, and 54.4% of the total HONO. Primary emissions appeared to contribute substantially more to the HONO budget during nighttime than that during daytime. This was very likely due to the fact that the BL was typically much lower at night and thus vehicle emissions were prone to accumulation. In addition, the observation site was located in the urban area, where heavy duty trucks were only allowed to operate at night.

To further evaluate the performance of the box model simulation on HONO concentration, we plotted the time series of both observed and simulated HONO in Fig. 5 for the entire campaign. Overall, the simulated HONO can basically match the measured HONO in terms of temporal profile and general trends with a correlation coefficient, $r = 0.76$. However, for some periods, the model significantly overestimated HONO, e.g., April 6-7 and 9-12. This was most likely due to precipitation events during these period, which make the parameters used in the simulation deviate away from the real values, overestimating the surface reactivities. For other cases, nighttime peaks of HONO were substantially higher than the measured ones, such as on April 3, 13, 19 and 23. One of the major reasons for these differences could be the error associated with the boundary layer height deduced from field measurements at nearby cites. Another significant source of error may be due to the fact that the surface properties may vary substantially. For example, the reported NO_2 reactive uptake coefficient was about 6×10^{-6} on humic acid aerosol surfaces under typical ambient conditions (Stemmler et al., 2007) and was about $(2.0 \pm 0.6)\times10^{-6}$ on soot surfaces (Monge et al., 2010). Moreover, Khalizov et al. (2010) found that the NO_2 uptake coefficient was within a range of $(1\text{-}5)\times10^{-5}$ on fresh laboratory-generated soot particles but it will be significantly reduced after coating the soot with sulfuric acid. Using TiO_2-SiO_2 mixture to represent mineral dusts, Ndour et al. (2008) found that NO_2 reactive uptake coefficient can range from $(0.12\text{-}1.9)\times10^{-6}$ with increasing relative content of TiO_2. Therefore, a single parameter can hardly represent all types of surface materials. During these events, organic matters consisted more than 40% of the total aerosol mass concentration. The corresponding NO_2 uptake coefficient may differ significantly from the literature value used in this work. Unfortunately, the aerosol surface properties were unknown in this work and, in fact, it unlikely can be determined directly, yet. More laboratory studies on the surface HONO formation are still critically needed to further constrain the uptake coefficient of NO_2 on various surfaces. Nevertheless, the uncertainties associated with nitrate photolysis and photo-enhanced heterogeneous conversion of NO_2 may also be partially responsible the differences between measured and simulated HONO due to their important roles as HONO sources under typical urban environments, often encountered in the central YRD region.

In this study, we have found that heterogeneous conversion of NO_2 on various surfaces dominated HONO production in this medium-sized city. During daytime, particulate nitrate may be photolyzed into HONO and contribute substantially to HONO budget. Although the study area is within the YRD region and populated with various industrial activities, no clear signs of industrial emissions, especially in terms of NO_x, could be identified. Instead, both NO_x and particulate nitrate displayed prominent rush hour peaks as shown in Fig. 2, with nitrate peaks built on top of a small level of background particulate nitrate, which was most likely converted from regional industrial NO_x emissions during the transport from the source location to the sample site (~20 km). Local automobile emissions evidently supplied most portion of the NO_x budget, the dominant precursor for HONO formation. Therefore, we believe industrial emissions did not impact the study area significantly. One possible reason is that NO_x emissions from the industrial sector have been well regulated in China, which is consistent with the findings that NO_x emissions in China have been significantly reduced (Li et al., 2017; van der A et al., 2017).

Meanwhile, a substantial portion of the freshly emitted NO_x from veichles was photochemically converted into HNO_3 and partitioned into the particle phase. Photolysis of nitrate, however, provided a nonnegligible route to recycle part of these non-reactive reservoir nitrogen-containing compounds back into the atmosphere in a highly reactive form, HONO. This can stimulate the atmospheric oxidative capacity by contributing to OH radical budget and catalyzing the photochemical reaction cycles. Therefore, stricter controls of automobile emissions may lead to extra benefits for the environment at this particular site.

In the past 5-10 years, emissions of some primary air pollutants (such as SO_2) have been significantly reduced in China due to the implementations of strict air pollution mitigation measures and regulations (Li et al., 2017; van der A et al., 2017). Although the emission standard for individual motor vehicle has been raised to the level of Euro VI in China, the vehicle population in China increased to 250 million units in June 2019, of which 198 million are private cars (http://autonews.gasgoo.com/china_news/70016117.html). Despite the reduction of NO_x emissions in the industrial sector, NO_x emissions from vehicle exhaust are still expected to continue to increase in the near future. Consequently, nitrate has been found to be the most abundant component of $PM_{2.5}$, surpassing sulfate (Sun et al., 2015; Tian et al., 2019). Our results implied that unlike the slow photolysis of gaseous HNO_3, the nitrate photolysis can provide a much faster and thus practical route to recycle nitrogen (in the form of HONO) back into the atmosphere. It can not only enhance the atmospheric oxidative capacity but also may promote the gas-phase photochemical reactions that can lead to O_3 and secondary aerosol formation. Therefore, regulation of automobile emissions should be given special attention during the establishment of air pollution mitigation strategies.

4. Conclusions and atmospheric implications

In this work, a comprehensive field campaign was conducted in Changzhou at an urban site typically found in the central YRD region in China to investigate the role of HONO on the atmospheric oxidation capacity. High levels of HONO were often observed during the observation period, with an average of 1.55±1.21 ppbv. At night, the observed NO_2-to-HONO conversion rate on average was about 0.018 h^{-1}. In addition, the average OH formation rates of the photolysis of HONO, O_3, HCHO and H_2O_2 along with ozonolysis of alkenes were determined to be 7.84×10^7, 2.02×10^7, 7.41×10^5, 3.79×10^5 and 1.51×10^6 molecules cm^{-3} s^{-1}, respectively. Evidently, HONO photolysis contributed a significant portion to the OH radical budget in the study area, especially on heavily polluted days when other important OH sources (such as O_3 photolysis) were suppressed. Formation of HONO and its subsequent photolysis is an important reaction route to sustain OH radical level in this kind of polluted environment. Accordingly, in order to mitigate the air pollution issues in the study area, it would be of particular importance to fully address the formation mechanisms of HONO. A MCM box model was utilized to evaluate the potential contributions from various HONO formation routes, including primary emissions from automobiles, homogeneous NO + OH reaction, heterogeneous reactions on both ground and aerosol surfaces and photolysis particulate nitrate. The emission factor of HONO from vehicle exhaust in the study area was estimated as the ratios of ΔHONO over ΔNO_x within the freshly emitted vehicle exhaust ($NO/NO_x > 0.85$) and a value of 0.69% was obtained and utilized in the model simulations. The results show that primary emissions contributed only a relatively small portion (12.3%) to the total HONO budget during daytime but a substantial portion (31.0%) at night. The gas-phase NO + OH reaction was the less important HONO source, with a contribution of 14.2% at night and 28.7% during the daytime. Heterogeneous reactions of NO_2 on various surfaces (mostly the ground surface) were responsible for most of the observed HONO, i.e., 34.7% during the day and 54.4% at night. Nevertheless, nighttime HONO can be reasonably explained by the aforementioned mechanisms. However, daytime HONO cannot be fully accounted for without the introduction of nitrate photolysis, which contributed about 24.1% of the daytime HONO according to the model simulation.

Our results indicate that nitrate photolysis can provide a more practical route than HNO_3 photolysis to recycle oxidized nitrogen species back into the gas phase, which not only can enhance atmospheric oxidative capacity in the form of HONO formation, but also may promote the formation of other secondary air pollutants (e.g., O_3) through NO_x-catalyzed photochemical reactions. Therefore, photolysis of particulate nitrate should be considered during the development of mitigation strategy for NO_x emissions.

Acknowledgements

This work is supported by the National Natural Science Foundation of China (41730106, 41575122, 91644213, 41675126 and 41975172) and the National Key Research and Development Project

(2017YFC0209501). The data used here are listed in the tables, figures and the supporting materials. The data used in this work are available from the authors upon request (zheng.jun@nuist.edu.cn).

References:

Acker, K., Febo, A., Trick, S., Perrino, C., Bruno, P., Wiesen, P., Moller, D., Wieprecht, W., Auel, R., Giusto, M., Geyer, A., Platt, U., Allegrini, I., 2006. Nitrous acid in the urban area of Rome. Atmos. Environ. 40, 3123-3133.

Alicke, B., Platt, U., Stutz, J., 2002. Impact of nitrous acid photolysis on the total hydroxyl radical budget during the Limitation of Oxidant Production/Pianura Padana Produzione di Ozono study in Milan. J. Geophys. Res. Atmos. 107, 8196.

Alicke, B., Geyer, A., Hofzumahaus, A., Holland, F., Konrad, S., Patz, H.W., Schafer, J., Stutz, J., Volz-Thomas, A., Platt, U., 2003. OH formation by HONO photolysis during the BERLIOZ experiment. J. Geophys. Res. Atmos. 108, 17.

Ammann, M., Kalberer, M., Jost, D.T., Tobler, L., Rossler, E., Piguet, D., Gaggeler, H.W., Baltensperger, U., 1998. Heterogeneous production of nitrous acid on soot in polluted air masses. Nature 395, 157-160.

Atkinson, R., Arey, J., 2003. Atmospheric degradation of volatile organic compounds. Chem. Rev. 103, 4605-4638.

Atkinson, R., Baulch, D.L., Cox, R.A., Crowley, J.N., Hampson, R.F., Hynes, R.G., Jenkin, M.E., Rossi, M.J., Troe, J., 2004. Evaluated kinetic and photochemical data for atmospheric chemistry: Volume I – gas phase reactions of Ox, HOx, NOx and SOx species. Atmos. Chem. Phys. 4, 1461-1738.

Bernard, F., Cazaunau, M., Grosselin, B., Zhou, B., Zheng, J., Liang, P., Zhang, Y., Ye, X., Daele, V., Mu, Y., Zhang, R., Chen, J., Mellouki, A., 2016. Measurements of nitrous acid (HONO) in urban area of Shanghai, China. Environ. Sci. Pollut. Res. Int. 23, 5818-5829.

Cui, L., Li, R., Zhang, Y., Meng, Y., Fu, H., Chen, J., 2018. An observational study of nitrous acid (HONO) in Shanghai, China: The aerosol impact on HONO formation during the haze episodes. Sci Total Environ 630, 1057-1070.

de Gouw, J., Warneke, C., 2007. Measurements of volatile organic compounds in the Earth's atmosphere using proton-transfer-reaction mass spectrometry. Mass Spectrom. Rev. 26, 223-257.

Dusanter, S., Vimal, D., Stevens, P.S., Volkamer, R., Molina, L.T., Baker, A., Meinardi, S., Blake, D., Sheehy, P., Merten, A., Zhang, R., Zheng, J., Fortner, E.C., Junkermann, W., Dubey, M., Rahn, T., Eichinger, B., Lewandowski, P., Prueger, J., Holder, H., 2009. Measurements of OH and HO2 concentrations during the MCMA-2006 field campaign – Part 2: Model comparison and radical budget. Atmos. Chem. Phys. 9, 6655-6675.

Elshorbany, Y.F., Kurtenbach, R., Wiesen, P., Lissi, E., Rubio, M., Villena, G., Gramsch, E., Rickard, A.R., Pilling, M.J., Kleffmann, J., 2009. Oxidation capacity of the city air of Santiago, Chile. Atmos. Chem. Phys. 9, 2257-2273.

Finlayson-Pitts, B.J., Pitts, J.N., 1999. Chemistry of the upper and lower atmosphere : theory, experiments and applications. Academic Press, San Diego, Calif.

Finlayson-Pitts, B.J., Wingen, L.M., Sumner, A.L., Syomin, D., Ramazan, K.A., 2003. The heterogeneous hydrolysis of NO_2 in laboratory systems and in outdoor and indoor atmospheres: An integrated mechanism. PCCP 5, 223-242.

Fuchs, H., Holland, F., Hofzumahaus, A., 2008. Measurement of tropospheric RO2 and HO2 radicals by a laser-induced fluorescence instrument. Rev. Sci. Instrum. 79, 084104.

Fuchs, H., Bohn, B., Hofzumahaus, A., Holland, F., Lu, K.D., Nehr, S., Rohrer, F., Wahner, A., 2011. Detection of HO2 by laser-induced fluorescence: calibration and interferences from RO2 radicals. Atmos. Meas. Tech. 4, 1209-1225.

George, C., Strekowski, R.S., Kleffmann, J., Stemmler, K., Ammann, M., 2005. Photoenhanced uptake of gaseous NO_2 on solid organic compounds: a photochemical source of HONO? Faraday Discuss. 130, 195-210.

Gerecke, A., Thielmann, A., Gutzwiller, L., Rossi, M.J., 1998. The chemical kinetics of HONO formation resulting from heterogeneous interaction of NO_2 with flame soot. Geophys. Res. Letts. 25, 2453-2456.

Gutzwiller, L., Arens, F., Baltensperger, U., Gäggeler, H.W., Ammann, M., 2002. Significance of Semivolatile Diesel Exhaust Organics for Secondary HONO Formation. Environ. Sci. Technol. 36, 677-682.

Han, C., Liu, Y., He, H., 2017. Heterogeneous reaction of NO_2 with soot at different relative humidity. Environ. Sci. Pollut. Res. 24, 21248–21255.

Han, C., Yang, W., Yang, H., Xue, X., 2017. Enhanced photochemical conversion of NO_2 to HONO on humic acids in the presence of benzophenone. Environ. Pollut. 231, 979-986.

He, S.Z., Chen, Z.M., Zhang, X., Zhao, Y., Huang, D.M., Zhao, J.N., Zhu, T., Hu, M., Zeng, L.M., 2010. Measurement of atmospheric hydrogen peroxide and organic peroxides in Beijing before and during the 2008 Olympic Games: chemical and physical factors influencing their concentrations. J. Geophys. Res. Atmos. 115, D17307.

Heland, J., Kleffmann, J., Kurtenbach, R., Wiesen, P., 2001. A New Instrument To Measure Gaseous Nitrous Acid (HONO) in the Atmosphere. Environ. Sci. Technol. 35, 3207-3212.

Hendrick, F., Müller, J.F., Clémer, K., Wang, P., De Mazière, M., Fayt, C., Gielen, C., Hermans, C., Ma, J.Z., Pinardi, G., Stavrakou, T., Vlemmix, T., Van Roozendael, M., 2014. Four years of ground-based MAX-DOAS observations of HONO and NO_2 in the Beijing area. Atmos. Chem. Phys. 14, 765-781.

Huang, R.-J., Yang, L., Cao, J., Wang, Q., Tie, X., Ho, K.-F., Shen, Z., Zhang, R., Li, G., Zhu, C., Zhang, N., Dai, W., Zhou, J., Liu, S., Chen, Y., Chen, J., O'Dowd, C.D., 2017. Concentration and sources of atmospheric nitrous acid (HONO) at an urban site in Western China. Sci. Total Environ. 593-594, 165-172.

Jarvis, D.L., Leaderer, B.P., Chinn, S., Burney, P.G., 2005. Indoor nitrous acid and respiratory symptoms and lung function in adults. Thorax 60, 474-479.

Jenkin, M.E., Saunders, S.M., Pilling, M.J., 1997. The tropospheric degradation of volatile organic compounds: a protocol for mechanism development. Atmos. Environ. 31, 81-104.

Jenkin, M.E., Young, J.C., Rickard, A.R., 2015. The MCM v3.3.1 degradation scheme for isoprene. Atmos. Chem. Phys. 15, 11433-11459.

Khalizov, A.F., Cruz-Quinones, M., Zhang, R., 2010. Heterogeneous Reaction of NO2 on Fresh and Coated Soot Surfaces. The Journal of Physical Chemistry A 114, 7516-7524.

Kirchstetter, T.W., Harley, A.R., Littlejohn, D., 1996. Measurement of nitrous acid in motor vehicle exhaust. Environ. Sci. Technol. 30, 2843–2849.

Kleffmann, J., Becker, K.H., Wiesen, P., 1998. Heterogeneous NO2 conversion processes on acid surfaces: possible atmospheric implications. Atmos. Environ. 32, 2721-2729.

Kleffmann, J., Gavriloaiei, T., Hofzumahaus, A., Holland, F., Koppmann, R., Rupp, L., Schlosser, E., Siese, M., Wahner, A., 2005. Daytime formation of nitrous acid: A major source of OH radicals in a forest. Geophys. Res. Letts. 32, L05818.

Kramer, L.J., Crilley, L.R., Adams, T.J., Ball, S.M., Pope, F.D., Bloss, W.J., 2019. Nitrous acid (HONO) emissions under real-world driving conditions from vehicles in a UK road tunnel. Atmos. Chem. Phys. Discuss. 2019, 1-31.

Kurtenbach, R., Becker, K.H., Gomes, J.A.G., Kleffmann, J., Lörzer, J.C., Spittler, M., Wiesen, P., Ackermann, R., Geyer, A., Platt, U., 2001. Investigations of emissions and heterogeneous formation of HONO in a road traffic tunnel. Atmos. Environ. 35, 3385-3394.

Lee, J.D., Whalley, L.K., Heard, D.E., Stone, D., Dunmore, R.E., Hamilton, J.F., Young, D.E., Allan, J.D., Laufs, S., Kleffmann, J., 2016. Detailed budget analysis of HONO in central London reveals a missing daytime source. Atmos. Chem. Phys. 16, 2747-2764.

Li, C., McLinden, C., Fioletov, V., Krotkov, N., Carn, S., Joiner, J., Streets, D., He, H., Ren, X., Li, Z., Dickerson, R.R., 2017. India Is Overtaking China as the World's Largest Emitter of Anthropogenic Sulfur Dioxide. Sci Rep 7, 14304.

Li, D., Xue, L., Wen, L., Wang, X., Chen, T., Mellouki, A., Chen, J., Wang, W., 2018. Characteristics and sources of nitrous acid in an urban atmosphere of northern China: Results from 1-yr continuous observations. Atmos. Environ. 182, 296-306.

Li, G., Lei, W., Zavala, M., Volkamer, R., Dusanter, S., Stevens, P., Molina, L.T., 2010. Impacts of HONO sources on the photochemistry in Mexico City during the MCMA-2006/MILAGO Campaign. Atmos. Chem. Phys. 10, 6551-6567.

Li, X., Brauers, T., Haseler, R., Bohn, B., Fuchs, H., Hofzumahaus, A., Holland, F., Lou, S., Lu, K.D., Rohrer, F., Hu, M., Zeng, L.M., Zhang, Y.H., Garland, R.M., Su, H., Nowak, A., Wiedensohler, A., Takegawa, N., Shao, M., Wahner, A., 2012. Exploring the atmospheric chemistry of nitrous acid (HONO) at a rural site in Southern China. Atmos. Chem. Phys. 12, 1497-1513.

Liang, Y., Zha, Q., Wang, W., Cui, L., Lui, K.H., Ho, K.F., Wang, Z., Lee, S.-c., Wang, T., 2017. Revisiting nitrous acid (HONO) emission from on-road vehicles: A tunnel study with a mixed fleet. J. Air Waste Manage. 67, 797-805.

Liu, Y., Lu, K., Li, X., Dong, H., Tan, Z., Wang, H., Zou, Q., Wu, Y., Zeng, L., Hu, M., Min, K.E., Kecorius, S., Wiedensohler, A., Zhang, Y., 2019. A Comprehensive Model Test of the HONO Sources Constrained to Field Measurements at Rural North China Plain. Environ Sci Technol 53, 3517-3525.

Lu, K.D., Rohrer, F., Holland, F., Fuchs, H., Bohn, B., Brauers, T., Chang, C.C., Häseler, R., Hu, M., Kita, K., Kondo, Y., Li, X., Lou, S.R., Nehr, S., Shao, M., Zeng, L.M., Wahner, A., Zhang, Y.H., Hofzumahaus, A., 2012. Observation and modelling of OH and HO2 concentrations in the Pearl River Delta 2006: a missing OH source in a VOC rich atmosphere. Atmos. Chem. Phys. 12, 1541-1569.

Ma, X., Tan, Z., Lu, K., Yang, X., Liu, Y., Li, S., Li, X., Chen, S., Novelli, A., Cho, C., Zeng, L., Wahner, A., Zhang, Y., 2019. Winter photochemistry in Beijing: Observation and model simulation of OH and HO2 radicals at an urban site. Sci. Total Environ. 685, 85-95.

Ma, Y., Diao, Y., Zhang, B., Wang, W., Ren, X., Yang, D., Wang, M., Shi, X., Zheng, J., 2016. Detection of formaldehyde emissions from an industrial zone in the Yangtze River Delta region of China using a proton transfer reaction ion-drift chemical ionization mass spectrometer. Atmos. Meas. Tech. 9, 6101-6116.

Michoud, V., Colomb, A., Borbon, A., Miet, K., Beekmann, M., Camredon, M., Aumont, B., Perrier, S., Zapf, P., Siour, G., Ait-Helal, W., Afif, C., Kukui, A., Furger, M., Dupont, J.C., Haeffelin, M., Doussin, J.F., 2014. Study of the unknown HONO daytime source at a European suburban site during the MEGAPOLI summer and winter field campaigns. Atmos. Chem. Phys. 14, 2805-2822.

Monge, M.E., D'Anna, B., Mazri, L., Giroir-Fendler, A., Ammann, M., Donaldson, D.J., George, C., 2010. Light changes the atmospheric reactivity of soot. Proc. Natl. Acad. Sci. USA 107, 6605-6609.

Müller, M., Anderson, B.E., Beyersdorf, A.J., Crawford, J.H., Diskin, G.S., Eichler, P., Fried, A., Keutsch, F.N., Mikoviny, T., Thornhill, K.L., Walega, J.G., Weinheimer, A.J., Yang, M., Yokelson, R.J., Wisthaler, A., 2016. In situ measurements and modeling of reactive trace gases in a small biomass burning plume. Atmos. Chem. Phys. 16, 3813-3824.

Nakashima, Y., Kajii, Y., 2017. Determination of nitrous acid emission factors from a gasoline vehicle using a chassis dynamometer combined with incoherent broadband cavity-enhanced absorption spectroscopy. Sci. Total Environ. 575, 287-293.

Ndour, M., D'Anna, B., George, C., Ka, O., Balkanski, Y., Kleffmann, J., Stemmler, K., Ammann, M., 2008. Photoenhanced uptake of NO_2 on mineral dust: Laboratory experiments and model simulations. Geophys. Res. Letts. 35, L05812.

Neuman, J.A., Trainer, M., Brown, S.S., Min, K.-E., Nowak, J.B., Parrish, D.D., Peischl, J., Pollack, I.B., Roberts, J.M., Ryerson, T.B., Veres, P.R., 2016. HONO emission and production determined from airborne measurements over the Southeast U.S. J. Geophys. Res. Atmos. 121, 9237–9250.

Nie, W., Ding, A.J., Xie, Y.N., Xu, Z., Mao, H., Kerminen, V.M., Zheng, L.F., Qi, X.M., Huang, X., Yang, X.Q., Sun, J.N., Herrmann, E., Petaja, T., Kulmala, M., Fu, C.B., 2015. Influence of biomass burning plumes on HONO chemistry in eastern China. Atmos. Chem. Phys. 15, 1147-1159.

Perner, D., Platt, U., 1979. Detection of nitrous-acid in the atmosphere by differential optical-absorption. Geophys. Res. Letts. 6, 917-920.

Petaja, T., Mauldin, R.L., Kosciuch, E., McGrath, J., Nieminen, T., Paasonen, P., Boy, M., Adamov, A., Kotiaho, T., Kulmala, M., 2009. Sulfuric acid and OH concentrations in a boreal forest site. Atmos. Chem. Phys. 9, 7435-7448.

Platt, U., Alicke, B., Dubois, R., Geyer, A., Hofzumahaus, A., Holland, F., Martinez, M., Mihelcic, D., Klupfel, T., Lohrmann, B., Patz, W., Perner, D., Rohrer, F., Schafer, J., Stutz, J., 2002. Free radicals and fast photochemistry during BERLIOZ. J. Atmos. Chem. 42, 359-394.

Qin, M., Xie, P., Su, H., Gu, J., Peng, F., Li, S., Zeng, L., Liu, J., Liu, W., Zhang, Y., 2009. An observational study of the HONO-NO_2 coupling at an urban site in Guangzhou City, South China. Atmos. Environ. 43, 5731-5742.

Ren, X., Harder, H., Martinez, M., Faloona, I.C., Tan, D., Lesher, R.L., Di Carlo, P., Simpas, J.B., Brune, W.H., 2004. Interference Testing for Atmospheric HOx Measurements by Laser-induced Fluorescence. J. Atmos. Chem. 47, 169-190.

Ren, X., Gao, H., Zhou, X., Crounse, J.D., Wennberg, P.O., Browne, E.C., LaFranchi, B.W., Cohen, R.C., McKay, M., Goldstein, A.H., Mao, J., 2010. Measurement of atmospheric nitrous acid at Blodgett Forest during BEARPEX2007. Atmos. Chem. Phys. 10, 6283-6294.

Ren, X.R., Harder, H., Martinez, M., Lesher, R.L., Oliger, A., Simpas, J.B., Brune, W.H., Schwab, J.J., Demerjian, K.L., He, Y., Zhou, X.L., Gao, H.G., 2003. OH and HO2 chemistry in the urban atmosphere of New York City. Atmos. Environ. 37, 3639-3651.

Rohrer, F., Lu, K., Hofzumahaus, A., Bohn, B., Brauers, T., Chang, C.-C., Fuchs, H., Häseler, R., Holland, F., Hu, M., Kita, K., Kondo, Y., Li, X., Lou, S., Oebel, A., Shao, M., Zeng, L., Zhu, T., Zhang, Y., Wahner, A., 2014. Maximum efficiency in the hydroxyl-radical-based self-cleansing of the troposphere. Nat. Geosci. 7, 559-563.

Rondon, A., Sanhueza, E., 1989. High HONO atmospheric concentrations during vegetation burning in the tropical savannah. Tellus B: Chem. Phys. Meteor. 41, 474-477.

Sarwar, G., Roselle, S.J., Mathur, R., Appel, W., Dennis, R.L., Vogel, B., 2008. A comparison of CMAQ HONO predictions with observations from the Northeast Oxidant and Particle Study. Atmos. Environ. 42, 5760-5770.

Scharko, N.K., Schutte, U.M., Berke, A.E., Banina, L., Peel, H.R., Donaldson, M.A., Hemmerich, C., White, J.R., Raff, J.D., 2015. Combined Flux Chamber and Genomics Approach Links Nitrous Acid Emissions to Ammonia Oxidizing Bacteria and Archaea in Urban and Agricultural Soil. Environ Sci Technol 49, 13825-13834.

Scharko, N.K., Martin, E.T., Losovyj, Y., Peters, D.G., Raff, J.D., 2017. Evidence for Quinone Redox Chemistry Mediating Daytime and Nighttime NO_2-to-HONO Conversion on Soil Surfaces. Environ. Sci. Technol. 51, 9633-9643.

Sleiman, M., Gundel, L.A., Pankow, J.F., Jacob, P., Singer, B.C., Destaillats, H., 2010. Formation of carcinogens indoors by surface-mediated reactions of nicotine with nitrous acid, leading to potential thirdhand smoke hazards. Proc. Natl. Acad. Sci. USA 107, 6576.

Spataro, F., Ianniello, A., Esposito, G., Allegrini, I., Zhu, T., Hu, M., 2013. Occurrence of atmospheric nitrous acid in the urban area of Beijing (China). Sci. Total Environ. 447, 210-224.

Stemmler, K., Ndour, M., Elshorbany, Y., Kleffmann, J., D'Anna, B., George, C., Bohn, B., Ammann, M., 2007. Light induced conversion of nitrogen dioxide into nitrous acid on submicron humic acid aerosol. Atmos. Chem. Phys. 7, 4237-4248.

Stutz, J., Alicke, B., Neftel, A., 2002. Nitrous acid formation in the urban atmosphere: Gradient measurements of NO_2 and HONO over grass in Milan, Italy. J. Geophys. Res. 107, 8192.

Su, H., Cheng, Y.F., Shao, M., Gao, D.F., Yu, Z.Y., Zeng, L.M., Slanina, J., Zhang, Y.H., Wiedensohler, A., 2008. Nitrous acid (HONO) and its daytime sources at a rural site during the 2004 PRIDE-PRD experiment in China. J. Geophys. Res. Atmos. 113, D14312.

Sun, Y.L., Wang, Z.F., Du, W., Zhang, Q., Wang, Q.Q., Fu, P.Q., Pan, X.L., Li, J., Jayne, J., Worsnop, D.R., 2015. Long-term real-time measurements of aerosol particle composition in Beijing, China: seasonal variations, meteorological effects, and source analysis. Atmos. Chem. Phys. 15, 10149-10165.

Tan, Z., Fuchs, H., Lu, K., Hofzumahaus, A., Bohn, B., Broch, S., Dong, H., Gomm, S., Häseler, R., He, L., Holland, F., Li, X., Liu, Y., Lu, S., Rohrer, F., Shao, M., Wang, B., Wang, M., Wu, Y., Zeng, L., Zhang, Y., Wahner, A., Zhang, Y., 2017. Radical chemistry at a rural site (Wangdu) in the North China Plain: observation and model calculations of OH, HO2 and RO2 radicals. Atmos. Chem. Phys. 17, 663-690.

Tan, Z., Rohrer, F., Lu, K., Ma, X., Bohn, B., Broch, S., Dong, H., Fuchs, H., Gkatzelis, G.I., Hofzumahaus, A., Holland, F., Li, X., Liu, Y., Liu, Y., Novelli, A., Shao, M., Wang, H., Wu, Y., Zeng, L., Hu, M., Kiendler-Scharr, A., Wahner, A., Zhang, Y., 2018. Wintertime photochemistry in Beijing: observations of ROx radical concentrations in the North China Plain during the BEST-ONE campaign. Atmos. Chem. Phys. 18, 12391-12411.

Tanner, D.J., Eisele, F.L., 1995. Present oh measurement limits and associated uncertainties. J. Geophys. Res. Atmos. 100, 2883-2892.

Tian, M., Liu, Y., Yang, F., Zhang, L., Peng, C., Chen, Y., Shi, G., Wang, H., Luo, B., Jiang, C., Li, B., Takeda, N., Koizumi, K., 2019. Increasing importance of nitrate formation for heavy aerosol pollution in two megacities in Sichuan Basin, southwest China. Environ. Pollut. 250.

Trick, S., 2004. Formation of nitrous acid on urban surfaces - a physicalchemical perspective. Ph.D. thesis, University of Heidelberg.

Trinh, H.T., Imanishi, K., Morikawa, T., Hagino, H., Takenaka, N., 2017. Gaseous nitrous acid (HONO) and nitrogen oxides (NO_x) emission from gasoline and diesel vehicles under real-world driving test cycles. J. Air Waste Manage. 67, 412-420.

van der A, R.J., Mijling, B., Ding, J., Koukouli, M.E., Liu, F., Li, Q., Mao, H., Theys, N., 2017. Cleaning up the air: effectiveness of air quality policy for SO2 and NOx emissions in China. Atmos. Chem. Phys. 17, 1775-1789.

VandenBoer, T.C., Brown, S.S., Murphy, J.G., Keene, W.C., Young, C.J., Pszenny, A.A.P., Kim, S., Warneke, C., de Gouw, J.A., Maben, J.R., Wagner, N.L., Riedel, T.P., Thornton, J.A., Wolfe, D.E., Dubé, W.P., Öztürk, F., Brock, C.A., Grossberg, N., Lefer, B., Lerner, B., Middlebrook, A.M., Roberts, J.M., 2013. Understanding the role of the ground surface in HONO vertical structure: High resolution vertical profiles during NACHTT-11. J. Geophys. Res. Atmos. 118, 10,155-110,171.

VandenBoer, T.C., Markovic, M.Z., Sanders, J.E., Ren, X., Pusede, S.E., Browne, E.C., Cohen, R.C., Zhang, L., Thomas, J., Brune, W.H., Murphy, J.G., 2014. Evidence for a nitrous acid (HONO) reservoir at the ground surface in Bakersfield, CA, during CalNex 2010. J. Geophys. Res. Atmos. 119, 9093-9106.

Wall, K.J., Harris, G.W., 2016. Uptake of nitrogen dioxide (NO_2) on acidic aqueous humic acid (HA) solutions as a missing daytime nitrous acid (HONO) surface source. J. Atmos. Chem. 74, 283-321.

Wang, J., Zhang, X., Guo, J., Wang, Z., Zhang, M., 2017. Observation of nitrous acid (HONO) in Beijing, China: Seasonal variation, nocturnal formation and daytime budget. Sci. Total Environ. 587-588, 350-359.

Wang, L., Wen, L., Xu, C., Chen, J., Wang, X., Yang, L., Wang, W., Yang, X., Sui, X., Yao, L., Zhang, Q., 2015. HONO and its potential source particulate nitrite at an urban site in North China during the cold season. Sci Total Environ 538, 93-101.

Wang, S., Zhou, R., Zhao, H., Wang, Z., Chen, L., Zhou, B., 2013. Long-term observation of atmospheric nitrous acid (HONO) and its implication to local NO_2 levels in Shanghai, China. Atmos. Environ. 77, 718-724.

Wong, K.W., Tsai, C., Lefer, B., Haman, C., Grossberg, N., Brune, W.H., Ren, X., Luke, W., Stutz, J., 2012. Daytime HONO vertical gradients during SHARP 2009 in Houston, TX. Atmos. Chem. Phys. 12, 635-652.

Xu, Z., Wang, T., Wu, J., Xue, L., Chan, J., Zha, Q., Zhou, S., Louie, P.K.K., Luk, C.W.Y., 2015. Nitrous acid (HONO) in a polluted subtropical atmosphere: Seasonal variability, direct vehicle emissions and heterogeneous production at ground surface. Atmos. Environ. 106, 100-109.

Ye, C., Zhou, X., Pu, D., Stutz, J., Festa, J., Spolaor, M., Tsai, C., Cantrell, C., Mauldin, R.L., Campos, T., Weinheimer, A., Hornbrook, R.S., Apel, E.C., Guenther, A., Kaser, L., Yuan, B., Karl, T., Haggerty, J., Hall, S., Ullmann, K., Smith, J.N., Ortega, J., Knote, C., 2016. Rapid cycling of reactive nitrogen in the marine boundary layer. Nature 532, 489-491.

Ye, C., Zhang, N., Gao, H., Zhou, X., 2017. Photolysis of Particulate Nitrate as a Source of HONO and NO_x. Environ. Sci. Technol. 51, 6849-6856.

Zhang, L., Wang, T., Zhang, Q., Zheng, J., Xu, Z., Lv, M., 2016. Potential sources of nitrous acid (HONO) and their impacts on ozone: A WRF-Chem study in a polluted subtropical region. J. Geophys. Res. Atmos. 121.

Zhang, W., Tong, S., Ge, M., An, J., Shi, Z., Hou, S., Xia, K., Qu, Y., Zhang, H., Chu, B., Sun, Y., He, H., 2019. Variations and sources of nitrous acid (HONO) during a severe pollution episode in Beijing in winter 2016. Sci. Total Environ. 648, 253-262.

Zheng, J., Shi, X., Ma, Y., Ren, X., Jabbour, H., Diao, Y., Wang, W., Ge, Y., Zhang, Y., Zhu, W., 2019. Contribution of HONO to the atmospheric oxidation capacity in an industrial zone in the Yangtze River Delta region of China. Atmos. Chem. Phys. Discuss. 2019, 1-47.

Zhou, X., Civerolo, K., Dai, H., Huang, G., Schwab, J., Demerjian, K., 2002. Summertime nitrous acid chemistry in the atmospheric boundary layer at a rural site in New York State. J. Geophys. Res. Atmos. 107, ACH 13-11-ACH 13-11.

Zhou, X., Gao, H., He, Y., Huang, G., Bertman, S.B., Civerolo, K., Schwab, J., 2003. Nitric acid photolysis on surfaces in low-NOxenvironments: Significant atmospheric implications. Geophys. Res. Letts. 30, 2217.

Zhou, X., Zhang, N., TerAvest, M., Tang, D., Hou, J., Bertman, S., Alaghmand, M., Shepson, P.B., Carroll, M.A., Griffith, S., Dusanter, S., Stevens, P.S., 2011. Nitric acid photolysis on forest canopy surface as a source for tropospheric nitrous acid. Nat. Geosci. 4, 440-443.

Ziemba, L.D., Dibb, J.E., Griffin, R.J., Anderson, C.H., Whitlow, S.I., Lefer, B.L., Rappenglück, B., Flynn, J., 2010. Heterogeneous conversion of nitric acid to nitrous acid on the surface of primary organic aerosol in an urban atmosphere. Atmos. Environ. 44, 4081-4089.

Table 1. The emission factors $\Delta HONO/\Delta NO_x$ within five fresh vehicle plumes in the early morning, *r* is the correlation coefficient between ΔHONO and ΔNO_x.

Start Time	Duration (min)	$\Delta NO/\Delta NO_x$	*r*	$\Delta HONO/\Delta NO_x$ (%)
2017/4/12 5:35	15	0.85	1.00	0.5748
2017/4/14 5:45	30	1.00	0.96	0.5627
2017/4/15 3:20	10	0.85	0.95	0.4130
2017/4/15 5:15	15	0.93	0.97	1.6326
2017/4/15 20:15	10	0.91	0.99	0.2714

Table 2. Parameters of HONO formation mechanisms used in the MCM box model.

Mechanism	**HONO formation formula**	**Parameter**	**References**
OH+NO	OH+NO→HONO	$k_{OH+NO}=9.8\times10^{-12}$ $cm^3\ molecule^{-1}\ s^{-1}$	(Atkinson et al., 2004)
direct emission		$HONO/NO_x = 0.69\%$	This work
NO_2+aerosol	NO_2+aerosol→0.5HONO	$\Upsilon_{NO2}=8\times10^{-6}$	(VandenBoer et al., 2013)
NO_2+ground	NO_2+ground→HONO	$\Upsilon_{NO2}=1\times10^{-5}$	(Scharko et al., 2015)
NO_2+aerosol+hv	NO_2+aerosol+hv→HONO	$\Upsilon_{NO_2} = 2\times10^{-5}\times\frac{J_{NO_2}}{J_{NO_2,noon}}$ $J_{NO_2,noon} = 0.005\ s^{-1}$	(Zhang et al., 2016)
NO_2+ground +hv	NO_2+ground+hv→HONO	$\Upsilon_{NO_2} = 6\times10^{-5}\times\frac{J_{NO_2}}{J_{NO_2,noon}}$ $J_{NO_2,noon} = 0.005s^{-1}$	(Wong et al., 2012)
NO_3^-→HONO	NO_3^-+hv→HONO	$J_{NO_3^-} = \frac{8.3\times10^{-5}}{7\times10^{-7}}\times J_{HNO_3}$	(Ye et al., 2017)

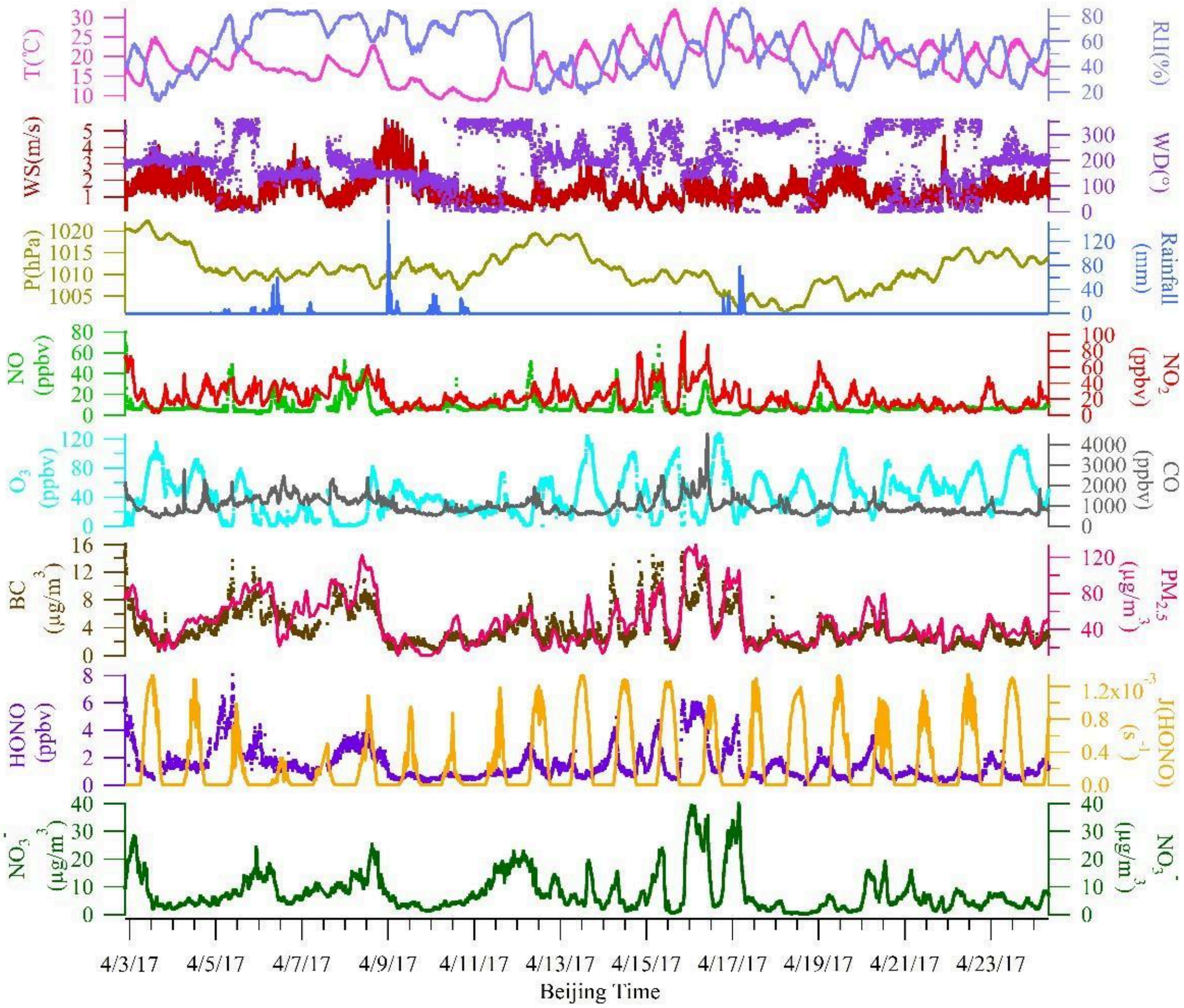

Figure 1. Time series of meteorological parameters (including ambient temperature (T), relative humidity (RH), wind speed (WS), wind direction(WD), pressure (P), and precipitation and measured NO, NO_2, O_3, CO, BC, $PM_{2.5}$ mass concentration, HONO, J(HONO) as well as particulate NO_3^- at an urban site in the Yangtze River Delta (YRD) region in China from April 3 to 24, 2017.

Figure 2. The box-whisker plots of diurnal profiles of NO_2, NO_x, HONO, aerosol surface density (S/V), particulate nitrate (NO_3^-) and HONO/NO_2 at an urban site in the Yangtze River Delta (YRD) region in China from April 3 to 24, 2017. On each box, the central mark is the median, the edges of the box are the 25th and 75th percentiles, the whiskers extend to the 5th and 95th percentiles. The solid circles are hourly means.

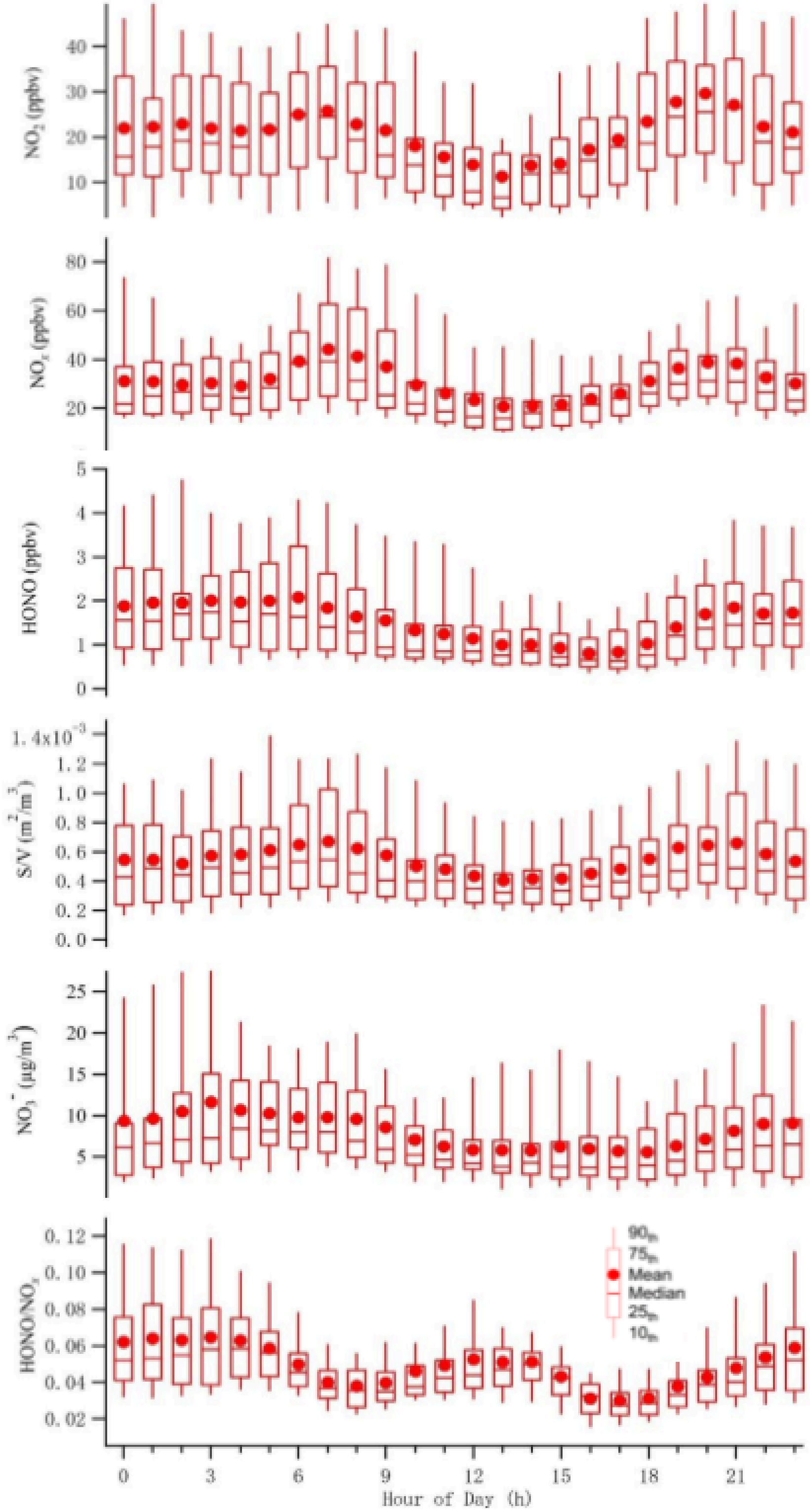

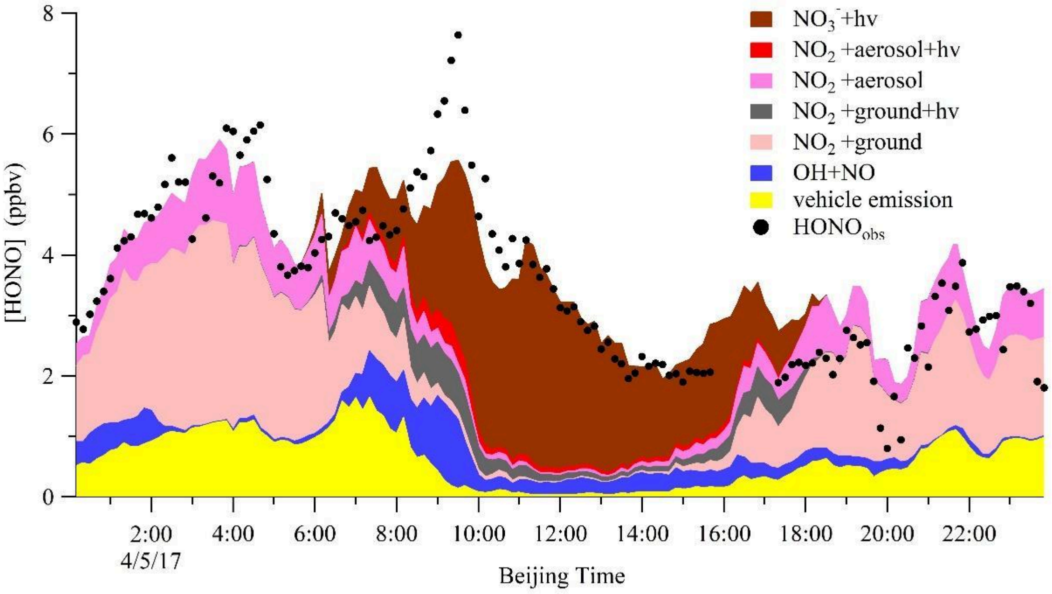

Figure 3. Time series of observed HONO (black dots) and simulated contributions from different sources to HONO on April 5th, 2017. The gap in the HONO observation from 16:00 to 17:00 was due to the instrument calibration.

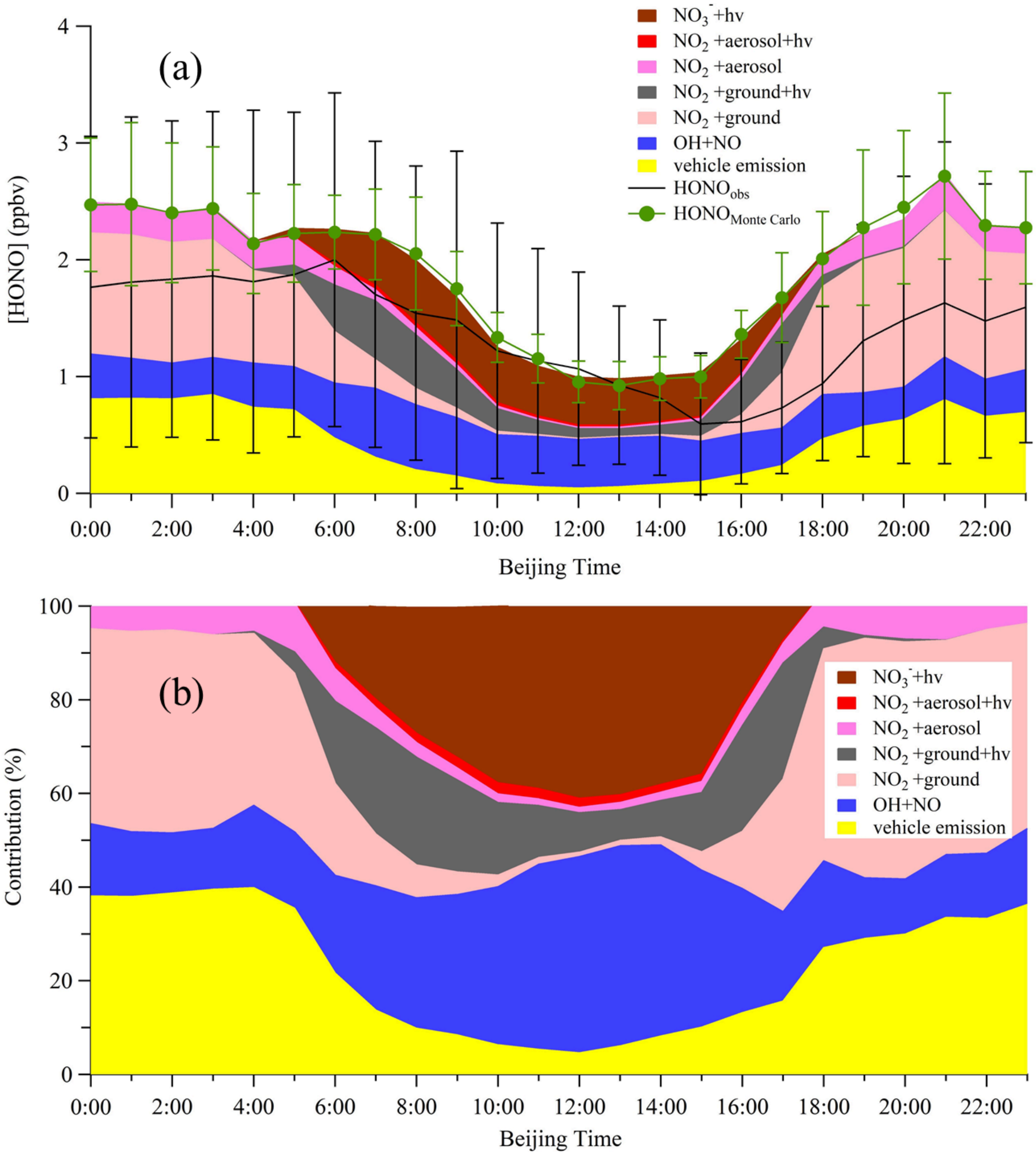

Figure 4. a) Diurnally averaged HONO and simulated contributions ofrom different sources to HONO for the campaign period. The black trace is the measured HONO and the black error bars represent one standard deviations (σ) of hourly averaged HONO concnetrations. The green markers are the averaged simulation results and the green error bars denote the Monte Carlo uncertainty analysis results; b) The diurnal contribution percentages of all HONO sources simulated by the model.

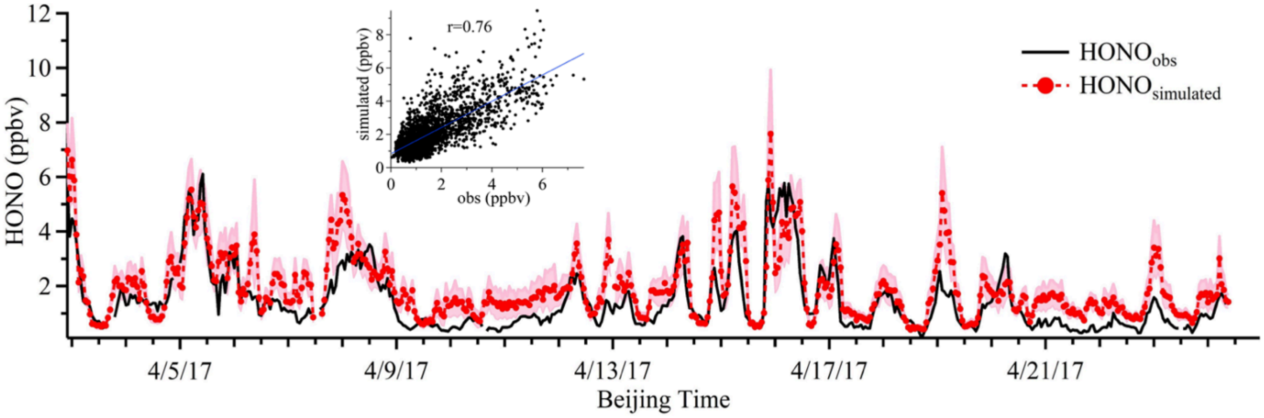

Figure 5. Time series of both observed (black) and simulated (red dots) HONO. The pink shaded area represents the uncertainty of simulation based on the Monte Carlo analysis. The insert shows the correlation between the observed and simulated HONO (r = 0.76).